Journal of Materials Chemistry A

PAPER

View Article Online
View Journal | View Issue

Cite this: J. Mater. Chem. A, 2015, 3, 11367

Three-dimensionally ordered macro-/mesoporous Ni as a highly efficient electrocatalyst for the hydrogen evolution reaction†

Tingting Sun,[a] Chengwei Zhang,[a] Jianfeng Chen,[a] Yushan Yan,[b] Anvar A. Zakhidov,[c] Ray H. Baughman[c] and Lianbin Xu*[a]

Received 21st February 2015
Accepted 13th April 2015

DOI: 10.1039/c5ta01383f

www.rsc.org/MaterialsA

Three-dimensionally (3D) ordered macro-/mesoporous (3DOM/m) Ni is fabricated by the chemical reduction deposition method using lyotropic liquid crystals (LLC) to template the mesostructure within the regular voids of a colloidal crystal (opal). The thereby achieved structural advantages of combining well-ordered bicontinuous mesopores with 3D interconnected periodic macropores, such as abundant exposed catalytically active sites, efficient mass transport, and high electrical conductivity, make this non-noble metal structure an excellent hydrogen evolution reaction (HER) electrocatalyst. The 3DOM/m Ni exhibits a low onset overpotential of 63 mV (*vs.* RHE) and a small Tafel slope of 52 mV per decade, as well as a long-term durability in alkaline medium. These distinct features of the 3DOM/m Ni render it a promising alternative to Pt-based HER electrocatalysts.

Introduction

Hydrogen, as a clean and appealing energy carrier, is advocated to be an ideal candidate to replace carbon-based fuels.[1] Sustainable hydrogen production by electrocatalytic water splitting is one of the important clean-energy technologies having great potential for using renewable energy sources.[2,3] The efficiency of the hydrogen evolution reaction (HER) in water electrolysis strongly depends on the electrocatalyst. To date, Pt and other precious metals are still the most effective HER electrocatalysts because they require low overpotentials and have fast kinetics for driving the HER.[4,5] However, the high cost and limited supply of noble metals make them less attractive for commercial applications.[6–8] Therefore, the substitution of rare and expensive noble metal electrocatalysts by earth-abundant materials would represent a significant step for the hydrogen-based energy industry.[9,10]

Among non-precious metal electrocatalysts, Ni and Ni-based metals have been shown to be promising alternatives to Pt-based catalysts for the HER in alkaline electrolytes because of their relatively high activity and stability.[11] To achieve a more active catalyst, one efficient way is to nanostructure the catalyst to significantly increase the number of catalytically active sites. A variety of nano or nanoporous structured Ni-based catalysts have been developed to catalyze the HER, such as three-dimensionally (3D) nanoporous Ni–Mo,[12] IrNiN nanoparticles,[13] nanoporous Ni films,[14] NiSe nanofibers,[15] 3D CoNiCu nanonetworks,[16] Ni–Mo nanopowders,[17] and Ni_2P nanoparticles.[18]

Owing to their periodic pore structure, uniform pore size in the mesoscale regime, high surface area and high electrical conductivity,[19] ordered mesoporous metals have shown superior performances for applications in diverse fields, including catalysis, magnetics, adsorption, and energy conversion and storage.[20–24] Several ordered mesoporous metals such as Pt,[25,26] Au,[27] Ru,[28] Ni[29] and their alloys with other metals[30,31] have been synthesized using different approaches based on hard templates (*e.g.* mesoporous silica) or soft templates (*e.g.* lyotropic liquid crystals (LLC) made of nonionic surfactants). However, the small windows of mesopores, which make it difficult for the pores to effectively transport guest molecules to the active sites located in internal mesopores, significantly limit applications of mesoporous metals. To overcome this problem, a promising strategy is to build hierarchical porous metallic nanostructures with interconnected macropores and mesopores, in which the macropores can facilitate mass transport and offset the diffusion limitations present in purely mesoporous metals while the mesopores enhance the surface area of the metals.[32–34]

Dual-template synthesis methods, which employ a combination of both colloidal crystal (opal) templating (hard-templating) and surfactant templating (soft-templating) techniques, are commonly used to fabricate hierarchical porous materials having 3D ordered macro- and mesoporous

[a]State Key Laboratory of Organic–Inorganic Composites, Beijing University of Chemical Technology, Beijing 100029, China. E-mail: xulb@mail.buct.edu.cn; Fax: +86-10-64434784; Tel: +86-10-64449241

[b]Department of Chemical and Biomolecular Engineering, University of Delaware, Newark, DE 19716, USA

[c]The Alan G. MacDiarmid NanoTech Institute, University of Texas at Dallas, Richardson, TX 75083, USA

† Electronic supplementary information (ESI) available. See DOI: 10.1039/c5ta01383f

structures.[35,36] Due to their ordered and tunable pore structures on both macroscale and mesoscale, 3D ordered macro-/mesoporous (3DOM/m) materials are of great interest for applications in catalysis, sensing, adsorption, and energy devices.[37–40] Reports have so far mainly focused on the fabrication of 3DOM/m carbon, silica and metal oxides,[41,42] but very few involved the production of 3DOM/m metals, even though nanometallic materials are among the most promising photoelectric and catalytic materials.[43] Recently, 3DOM/m Pt materials were prepared by electrochemical or chemical reduction of Pt ions in the LLC filled inside the opals.[44,45] The LLC was formed by infiltrating the ethanol/water solution of a nonionic surfactant and H_2PtCl_6 into the void spaces of the opal, followed by preferential evaporation of ethanol to allow self-assembly of the surfactant molecules inside the opal. The LLC-filled opal was then used as a dual-template for the fabrication of 3DOM/m Pt with the LLC and opal as a soft template for mesopores and a hard template for macropores, respectively.

To our knowledge, no metal with the 3DOM/m structure, except Pt, has been previously prepared and studied. Herein, we extend the dual-templating technique to synthesize 3DOM/m Ni monoliths. To accomplish this we used the poly(methyl methacrylate) (PMMA) opal as the macroporous mold and the LLC of the nonionic surfactant Brij 58 ($C_{16}H_{33}(OCH_2CH_2)_{20}OH$) as the meso-structural template. A high concentration aqueous precursor solution containing Brij 58 and the nickel salt ($NiCl_2 \cdot 6H_2O$) used as the Ni source was first infiltrated into the pores of the PMMA opal monolith and then self-assembled to form the LLC. Subsequent chemical reduction deposition of Ni and removal of the templates (PMMA opal and Brij 58) produced hierarchically ordered porous Ni with well-defined macropores and mesopores. In addition, the HER catalytic properties of the prepared 3DOM/m Ni in aqueous alkaline medium are evaluated in detail.

Results and discussion

Structural and morphological characterization

Fig. 1a shows a typical scanning electron microscopy (SEM) image of the PMMA colloidal crystal (opal) monolith consisting of highly ordered close-packed PMMA spheres with *ca.* 330 nm diameter. Different regions corresponding to (111) and (100) orientations can be observed. The low-magnification SEM image of 3DOM/m Ni (Fig. 1b) shows that the opal replica structure has an ordered 3D-interconnected porous architecture containing open windows between pores. The inset of Fig. 1b is a higher magnification image of the predominately (111) orientation of the 3DOM/m Ni. The size of the macropores (~330 nm) is consistent with the diameter of the original PMMA spheres, indicating that the 3DOM/m Ni does not contract during removal of the opal template. Fig. S1a† provides a high

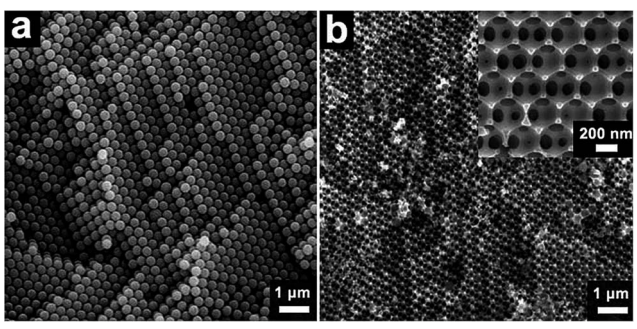

Fig. 1 SEM images of (a) the PMMA opal consisting of 330 nm diameter spheres, and (b) 3DOM/m Ni after the removal of the opal template, inset: higher magnification with (111) orientation.

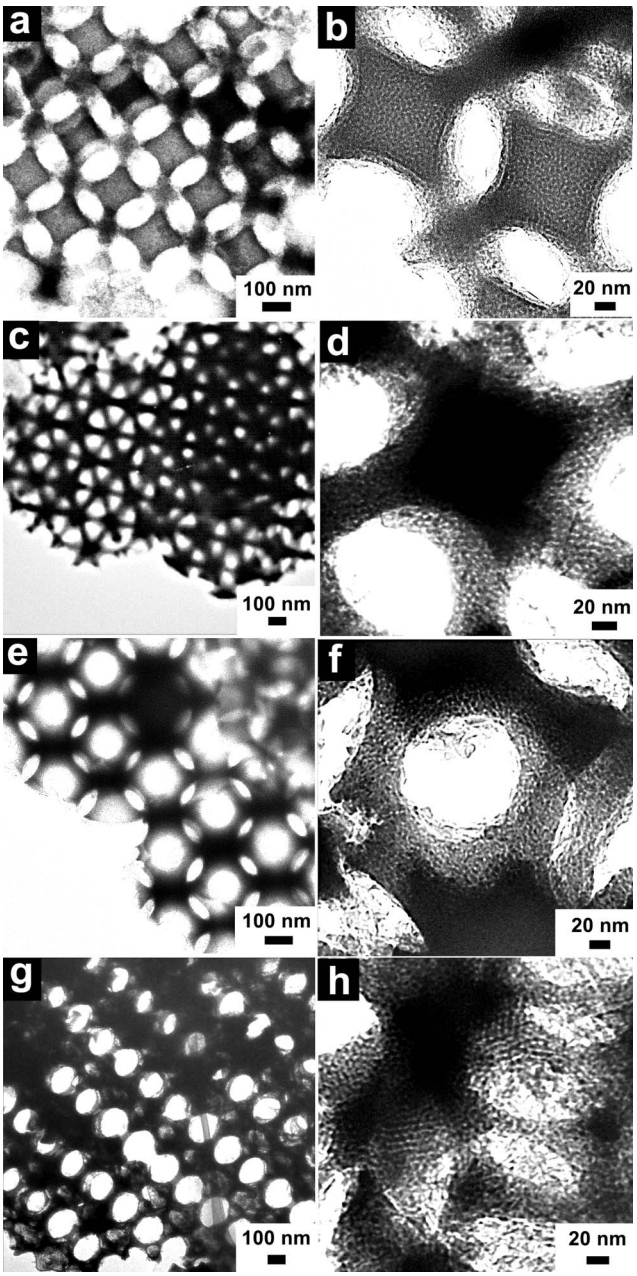

Fig. 2 TEM images of 3DOM/m Ni viewed along (a) (100), (c) (111), (e) (110), and (g) (211) directions. (b, d, f and h) High-resolution TEM images corresponding to (a, c, e and g), respectively, showing the Ni mesostructure.

magnification image of a (100) plane for 3DOM Ni, again indicating a highly periodic structure.

More detailed structural information of the 3DOM/m Ni was obtained by transmission electron microscopy (TEM) and high-resolution TEM (HR-TEM). Fig. 2a, c, e and g show the TEM images of as-prepared 3DOM/m Ni in the (100), (111), (110) and (211) directions, respectively. The ordered face-centered cubic (fcc) macropores are uniform and the pore size is around 330 nm, which is consistent with the observation from the SEM images. The corresponding HR-TEM images (Fig. 2b, d, f and h) reveal that well-defined mesopores are located in the macropore walls, indicating the hierarchically ordered macro/mesoporous structure of the 3DOM/m Ni. The mesopore diameter is in the 3–5 nm range and the average size of the Ni particles is approximately 4 nm, which is smaller than that for the 3DOM Ni (~8 nm, Fig. S1b†) and the Ni NPs (~10 nm, Fig. S2b†) used for comparative studies of catalytic activity. The distance between neighboring mesopores of the 3DOM/m Ni is estimated to be 7–8 nm.

The nitrogen adsorption/desorption isotherm of as-prepared 3DOM/m Ni is shown in Fig. 3. The isotherm can be classified as type IV, indicative of the presence of a mesoporous structure according to the IUPAC nomenclature.[46] The Brunauer–Emmett–Teller (BET) surface area and pore volume of the 3DOM/m Ni are 116 $m^2\ g^{-1}$ and 0.31 $cm^3\ g^{-1}$, respectively. The inset of Fig. 3 shows the pore size distribution of the 3DOM/m Ni calculated by the Barrett–Joyner–Halenda (BJH) method using the desorption isotherm. The average pore diameter of the mesoporous Ni is 3.9 nm. In addition, the mesopore size distribution is in the range of 3–5 nm, and such a narrow distribution implies substantial homogeneity of the mesopores for the Ni macropore walls. The BJH derived pore size distribution corresponds closely to the HR-TEM results.

Inductively coupled plasma-atomic emission spectrometry (ICP) analysis demonstrated that the 3DOM/m Ni, 3DOM Ni, and Ni NPs contain ~6 wt% boron. Fig. 4a and S3† show the wide-angle XRD patterns of these Ni samples. In each XRD pattern, a broad diffraction peak at around $2\theta = 45°$ is observed, suggesting that the incorporation of the B phase in these as-prepared Ni catalysts results in an amorphous-like state.[47] The selected-area electron diffraction (SAED) pattern of the 3DOM/m Ni (Fig. S4†) exhibits halo rings rather than distinct points, in agreement with the XRD analysis. No Ni oxide diffraction is observed from the SAED pattern, indicating that Ni is present in the metallic state in the sample, as is consistent with that reported for mesostructured Ni-based alloys.[22] The small-angle XRD (SAXRD) pattern (Fig. 4b) of the 3DOM/m Ni exhibits a peak at around $2\theta = 1.3°$, which can be assigned to the (100) diffraction of the hexagonal mesoscale structure with a *d*-spacing of 6.7 nm. The presence of this SAXRD peak indicates the formation of an ordered mesostructure in the 3DOM/m Ni. The distance between the mesopores, estimated from the (100) diffraction peak, is 7.7 nm ($6.7\ nm \times 2/\sqrt{3}$), which coincides with the HR-TEM observations.

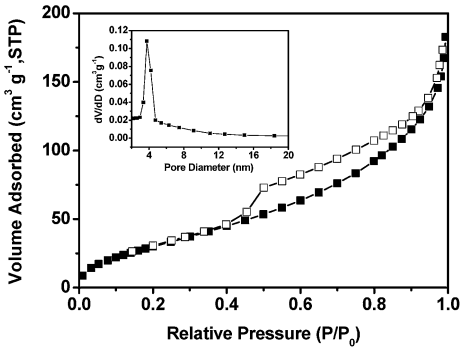

Fig. 3 Nitrogen adsorption/desorption isotherm and pore size distribution curve (inset) for 3DOM/m Ni.

Electrochemical measurements for characterizing the HER

The HER polarization curves (*j*–*V* plots) of the samples measured in 1.0 M NaOH solution at a scan rate of 2 mV s^{-1} and a rotating speed of 2000 rpm are shown in Fig. 5a for the different samples. As expected, the commercial Pt/C catalyst used for base-line comparison showed excellent HER activity, providing a near-zero overpotential. The 3DOM/m Ni provides a small onset overpotential of ~63 mV, beyond which the cathodic current rises rapidly under more negative potentials. In sharp contrast, 3DOM Ni and Ni NPs show much larger onset overpotentials of ~101 mV and ~112 mV, respectively, and a bare GC electrode exhibits almost no catalytic activity for the HER. To drive a cathodic current density of −10 mA cm^{-2}, the 3DOM/m Ni only requires an overpotential (η) of 171 mV, which

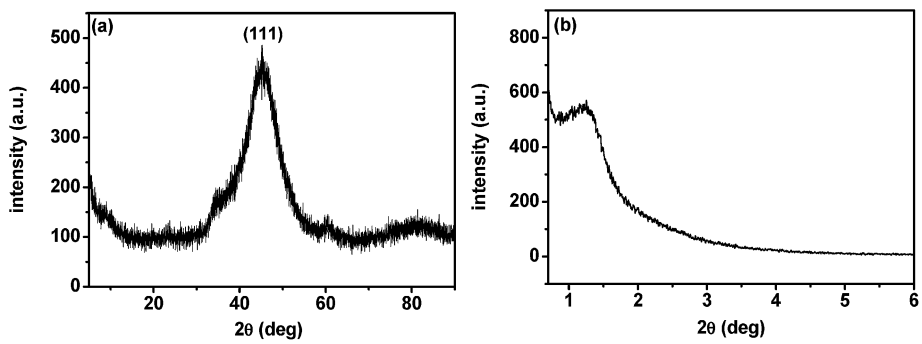

Fig. 4 (a) Wide-angle and (b) low-angle X-ray diffraction patterns of 3DOM/m Ni.

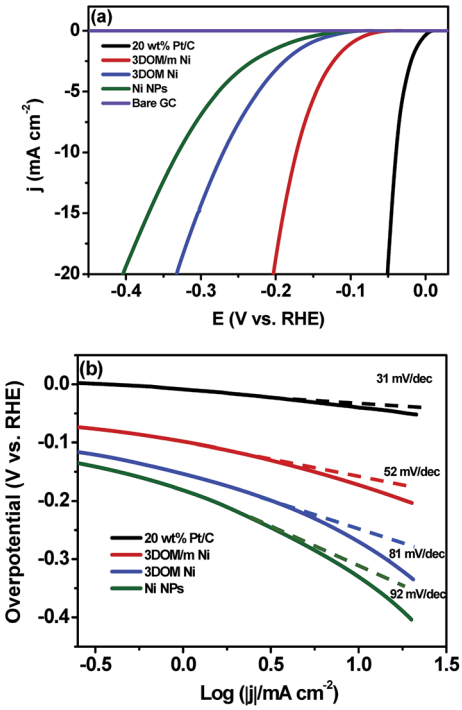

Fig. 5 (a) Polarization curves for the HER on a bare glassy carbon (GC) electrode and modified GC electrodes comprising Pt/C, 3DOM/m Ni, 3DOM Ni, and Ni NPs in 1.0 M NaOH solution at a scan rate of 2 mV s^{-1}. (b) Tafel plots derived from (a).

is much smaller than those exhibited by the 3DOM Ni (270 mV) and Ni NPs (331 mV) electrodes. Also, this overpotential (171 mV) of the 3DOM/m Ni at −10 mA cm^{-2} is comparable to or smaller than that of other reported non-Pt HER electrocatalysts operating in alkaline aqueous solutions, including the Ni inverse opal (~240 mV),[48] bulk Mo_2C (~200 mV) and MoB (~220 mV),[49] Ni_2P nanoparticles (~180 mV),[50] porous Mo_2C nanorods (~150 mV),[51] Ni_3S_2/carbon nanotube composite (~350 mV),[52] and Ni_xCo_{10-x}/C nanoflakes (~370 mV),[53] suggesting that the 3DOM/m Ni is a relatively super catalyst for the HER.

The Tafel plots of these samples (Fig. 5b), obtained by plotting the overpotential *versus* the log(cathodic current density), fit well with the Tafel equation ($\eta = b\log(j) + a$, where j is the current density and b is the Tafel slope). The Tafel slope is an inherent property of the catalyst, and a smaller one means a faster increase of HER rate with increasing potential. The commercial Pt/C exhibits a Tafel slope of 31 mV per decade, which is consistent with reported values.[50] The 3DOM/m Ni, 3DOM Ni, and Ni NPs show the Tafel slopes of 52, 81, and 92 mV per decade, respectively, indicating that 3DOM/m Ni has the highest HER activity among the three samples. This Tafel slope of 52 mV per decade is lower than or comparable to those observed for the other nanostructured non-precious metal HER catalysts, such as Ni_2P nanoparticles[18] (~70 mV per decade), NiSe nanofibers[54] (~64 mV per decade), 3D nanoporous CoP nanowires[55] (~65 mV per decade), nanoporous Mo_2C nanowires[56] (~53 mV per decade), MoS_2 nanoparticles on mesoporous graphene foams[57] (~42 mV per decade), MoO_3–MoS_2 nanowires[58] (~50–60 mV per decade), MoS_2/ordered mesoporous carbon nanospheres[59] (~41 mV per decade), and double-gyroid MoS_2 films[60] (~50 mV per decade).

It is known that the Tafel slope is determined by the rate-limiting step of the HER.[61] According to the two-electron-reaction models, the HER in aqueous alkaline solution proceeds in the following three possible principle steps:[62,63]

Discharge step – Volmer reaction

$$H_2O + M + e^- \rightarrow MH_{ads} + OH^-,\ b = 2.3RT/\alpha nF \sim 120\ \text{mV}$$

Desorption – Heyrovsky reaction

$$H_2O + MH_{ads} + e^- \rightarrow H_2 + M + OH^-,\ b = 2.3RT/(1+\alpha)F \sim 40\ \text{mV}$$

Recombination – Tafel reaction

$$MH_{ads} + MH_{ads} \rightarrow H_2 + 2M,\ b = 2.3RT/2F \sim 30\ \text{mV}$$

In the above equations, M represents a free active site on the metal surface, MH_{ads} is the metal surface involving an adsorbed H intermediate, R is the ideal gas constant, T is the absolute temperature, $\alpha \sim 0.5$ is the symmetry coefficient, and F is the Faraday constant. If the discharge process (Volmer reaction) is the rate determining step, a slope of 120 mV per decade should be observed. On the other hand, a Tafel slope of 40 or 30 mV per decade would be expected when the Heyrovsky or Tafel reaction acts as the rate limiting step, respectively. The observed Tafel slope of 52 mV per decade for the 3DOM/m Ni suggests that the Volmer–Heyrovsky mechanism with the electrochemical

Table 1 Onset overpotential, Tafel slope, exchange current density (j_0), and charge transfer resistance (R_{ct}) of different catalysts

Catalyst	Onset overpotential (mV)	Tafel slope (mV per decade)	Exchange current density (mA cm^{-2})	R_{ct}/η= 100 mV (Ω cm^2)
20 wt% Pt/C	0	31	0.73	—
3DOM/m Ni	63	52	0.11	33
3DOM Ni	101	81	1.2×10^{-2}	320
Ni NPs	112	92	8.9×10^{-3}	772

desorption as the rate-determining step is operative in the 3DOM/m Ni catalyzed HER.

The exchange current density (j_0), calculated by the Butler–Volmer equation,[64] is considered a reasonable measure of the catalytic efficiency for the HER. Table 1 lists the j_0 values of the samples. The j_0 for the 3DOM/m Ni is determined as 0.11 mA cm^{-2}, which is within the same order of magnitude as that of the commercial Pt/C catalyst (0.73 mA cm^{-2}), and much higher than those of some other reported HER catalysts summarized in Table S1.†

Electrochemical impedance spectroscopy (EIS) measurements were conducted to study the electrode kinetics under HER operating conditions. Fig. 6a displays the Nyquist plots collected at an overpotential of η = 100 mV for the various electrodes. The EIS data were fitted to an equivalent circuit according to the model of the simple Randles cell (inset of Fig. 6a). The observed one semicircle in the Nyquist plot suggests that the charge-transfer process controls the kinetics at the electrode interface. It is well accepted that the diameter of the semicircle reflects the charge-transfer resistance (R_{ct}) of the porous electrode.[65] The 3DOM/m Ni electrode exhibits a R_{ct} of 33 Ω cm^2, which is much lower than that of the 3DOM Ni (320 Ω cm^2) and Ni NPs (772 Ω cm^2), demonstrating the higher charge transport efficiency of the 3DOM/m Ni. The Nyquist plot for the 3DOM/m Ni at the selected overpotentials ranging from 0 to 200 mV, which is almost located in the linear portion of the Tafel plots, is presented in Fig. 6b. The diameter of the semicircle reduces with increase in overpotential, indicating faster charge transfer kinetics for the HER at higher overpotentials.

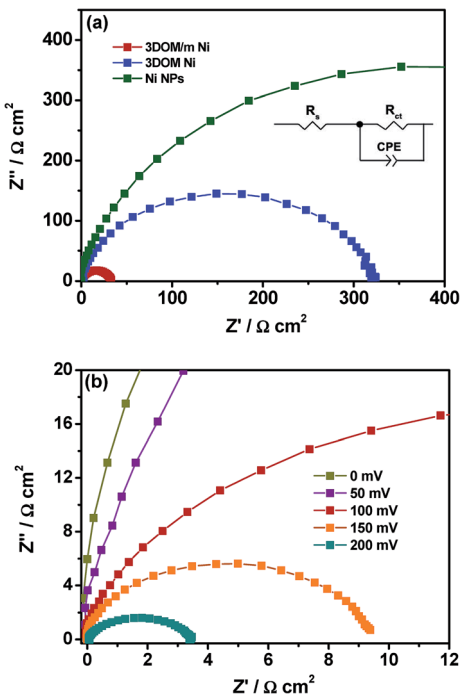

Fig. 6 (a) Nyquist plots of 3DOM/m Ni, 3DOM/m Ni, and Ni NPs recorded at η = 100 mV *vs.* RHE in 1.0 M NaOH solution, inset: equivalent circuit used to fit the EIS data. (b) Nyquist plots collected on 3DOM/m Ni at selected overpotentials.

The highly active electrocatalytic performance of the 3DOM/m Ni for the HER is likely related to the following factors: (1) the ordered mesopores with high surface area provide more catalytically active sites for the HER;[60] (2) the 3D ordered interconnected macro/mesoporous structure improves the utilization efficiency of active sites by facilitating the mass transport of fluids and enhancing the access of reactant molecules to the active sites;[66–68] and (3) the 3D interconnected framework with ordered macropores and mesopores can promote electron transport and facilitate ion diffusion, and thus increase the conductivity, leading to improved HER kinetics.[69,70]

The durability is also an essential criterion for a practical electrocatalyst. In this study, the durability tests of the 3DOM/m Ni, 3DOM Ni, and Ni NPs catalysts were carried out by cycling the electrode potential between −0.3 and +0.2 V *vs.* RHE at a scan rate of 100 mV s^{-1} for 2000 cycles. As seen in Fig. 7a, the polarization curve of the 3DOM/m Ni was little affected by cycling. The inset of Fig. 7a shows the time-dependent catalytic overpotential curve for the 3DOM/m Ni under a static current density of −10 mA cm^{-2}. After 25 hours of continuous operation, the catalytic overpotential shows a negligible increase, suggesting that the 3DOM/m Ni catalyst has superior stability in the long-term electrochemical process compared with some other recently reported HER catalysts, such as nanoscale NiO/Ni

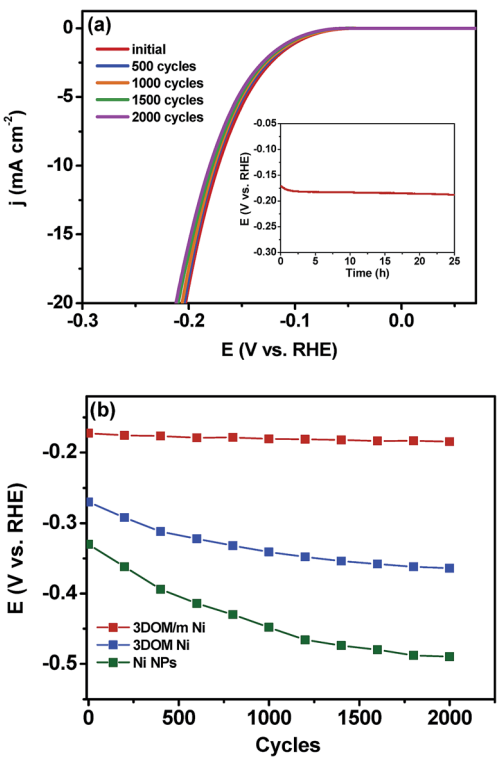

Fig. 7 (a) Polarization curves of 3DOM/m Ni in 1.0 M NaOH solution initially and after 500, 1000, 1500, and 2000 CV sweeps between −0.3 and 0.2 V *vs.* RHE, inset: time-dependent catalytic overpotential curve for 3DOM/m Ni at a static current density of −10 mA cm^{-2} for 25 hours. (b) Potential values recorded initially and after every 200 CV sweeps from the polarization curves of durability measurements for 3DOM/m Ni, 3DOM Ni, and Ni NPs at −10 mA cm^{-2}.

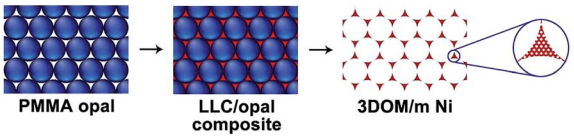

Scheme 1 Schematic of the preparation of the 3D ordered macro-/mesoporous (3DOM/m) Ni.

heterostructures,[71] CoP nanoparticles,[72] and FeP nanorod arrays.[73] Furthermore, from the potential values at a current density of −10 mA cm^{-2} before and after the test (Fig. 7b), the 3DOM/m Ni exhibits high durability with only a 6.9% increase of the overpotential, while 3DOM Ni shows a larger overpotential increase of 34.8% and Ni NPs produce even a greater overpotential increase of 48.5%. These results demonstrate that the 3DOM/m Ni catalyst has higher stability than the 3DOM Ni and Ni NPs under alkaline conditions. The high durability of the 3DOM/m Ni catalyst may be attributed to its unique 3D interconnected macro- and mesoporous framework structure, which has higher stability against growth and agglomeration of Ni particles, as well as the nanoparticle separation from the electrode that can occur for aggregated Ni nanoparticles.[74–77]

Conclusions

In summary, a 3D ordered macro-/mesoporous (3DOM/m) Ni catalyst has been successfully synthesized by employing a dual templating approach, using the PMMA opal as a macropore template and lyotropic liquid crystals (LLC) of the nonionic surfactant Brij 58 as a mesopore template. The macropore walls of the prepared 3DOM/m Ni exhibit a well-defined mesoporous structure with a narrow pore size distribution of 3–5 nm. As a result of the high surface area of the mesopores, efficient mass transport and increased accessible surface area from the macropores, and improved conductivity from the 3D interconnected network structure, the 3DOM/m Ni shows greatly enhanced electrocatalytic performance for the hydrogen reduction reaction (HER) compared to the 3D ordered macroporous (3DOM) Ni and Ni nanoparticles (NPs). The as-prepared 3DOM/m Ni electrocatalyst exhibited a low onset overpotential of 63 mV (*vs.* RHE), a low Tafel slope of 52 mV per decade, a high exchange current density of 0.11 mA cm^{-2} and a low charge transfer resistance of 33 Ω cm^2 at an overpotential of 100 mV, as well as a good durability with a negligible activity loss after 2000 CV cycles in alkaline medium. The excellent catalytic activity and stability demonstrate that the 3DOM/m Ni could be a promising alternative to Pt-based HER electrocatalysts. Also, this novel 3D hierarchical ordered porous Ni may potentially be used in other applications, such as magnetics, batteries, adsorption, separation, and catalytic hydrogenation.

Experimental section

Chemicals

Methyl methacrylate (MMA, 99%), nonionic surfactant Brij 58 ($C_{16}H_{33}(OCH_2CH_2)_{20}OH$), dimethylamine borane (DMAB) ($(CH_3)_2NHBH_3$, 97%), and Nafion solution (5 wt%) were purchased from Sigma-Aldrich Co. 2,2′-Azobis(2-methylpropionamidine)dihydrochloride (AAPH, 98%) was bought from J&K Chemical Ltd. Nickel(II) chloride hexahydrate ($NiCl_2 \cdot 6H_2O$, 98%), sodium hydroxide (NaOH, 96%), tetrahydrofuran (THF, 99%), and ethanol (99.7%) were obtained from Beijing Chemical Works. All chemicals were used as received without further purification.

Preparation of PMMA colloidal crystal (opal) monoliths

Monodispersed PMMA spheres were synthesized by emulsifier-free emulsion polymerization of MMA for about two hours at 70 °C using AAPH as an initiator, as reported by Stein *et al.* previously.[78] The resulting PMMA sphere suspension was then transferred to a wide mouth glass bottle and left for about 2 months at room temperature thereby allowing the spheres to completely precipitate. After that, the supernatant liquid was carefully removed using a dropper without disturbing the precipitate, and then the precipitate was kept in open air at room temperature (~10 days) for complete evaporation of the remaining water to form PMMA opal monoliths. The prepared PMMA opal monoliths were heated at 120 °C for 15 minutes to strengthen contact between each of the spheres. The PMMA opals in this study are composed of ~330 nm diameter PMMA spheres.

Synthesis of 3D ordered macro-/mesoporous (3DOM/m) Ni catalysts

The synthetic procedure for the 3DOM/m Ni is illustrated in Scheme 1. To make a templating precursor, 5.0 g Brij 58 was added to a solution containing 3.0 g $NiCl_2 \cdot 6H_2O$ and 2.8 g water, and the concentration of Brij 58 was adjusted to be 55 wt% (Brij 58/(water + Brij 58)). The obtained mixture was heated to 80 °C and stirred until a homogeneous green color mixture was produced. A closed container was used to avoid evaporation of the water. Then the mixture was infiltrated within the void spaces of the PMMA opal template by immersing the opal in the mixture for 5 hours at 80 °C. After cooling to room temperature, the LLC was formed and the pores of the PMMA opal were filled with LLC containing Ni^{2+}. Subsequently, the LLC-filled PMMA opal was carefully removed from the bulk LLC phase, and put in a closed vial with the reducing agent DMAB (~0.8 g) in a small dish. The vial was then kept at 25 °C for 3 days, allowing the LLC-filled opal to be exposed to saturated DMAB vapor under autogenous pressure. During the process, the Ni^{2+} was gradually reduced by the infiltration of DMAB vapor into the LLC-Ni^{2+}/opal composite. After the deposition of Ni, the sample was treated with THF, ethanol, and deionized water to remove the PMMA opal and surfactants to produce the freestanding 3DOM/m Ni.

Synthesis of 3D ordered macroporous (3DOM) Ni

The PMMA opal monolith was first immersed in a Ni solution containing 3.0 g $NiCl_2 \cdot 6H_2O$, 3.0 g water, and 5.0 g ethanol for 5 hours at room temperature. Then, the chemical reduction deposition of Ni was conducted in the DMAB bath following the

procedure described above for preparing the 3DOM/m Ni. Subsequent removal of the PMMA opal template by THF produced freestanding 3DOM Ni.

Synthesis of Ni nanoparticles (NPs)

3.0 g $NiCl_2 \cdot 6H_2O$ was dissolved in 2.8 g water to prepare the Ni solution used for Ni nanoparticle deposition. The chemical reduction of Ni^{2+} was performed by adding 0.6 g DMAB into the Ni solution and then allowing reaction at 25 °C for 1 day. The resulting precipitate was centrifuged, washed with deionized water and ethanol, and then dried at 25 °C in a vacuum overnight to obtain Ni NPs.

Characterization

Scanning electron microscopy (SEM) images were obtained on a Hitachi S-4700 FEG scanning electron microscope. Transmission electron microscopy (TEM) and selected-area electron diffraction (SAED) were carried out on a JEOL JEM-3010 transmission electron microscope operating at 200 kV. Powder X-ray diffraction (XRD) data were collected on a Rigaku D/max 2500 VB2+/PC diffractometer with Cu-Kα radiation (λ = 1.5418 Å). Nitrogen adsorption and desorption isotherms were measured at 77 K using Micromeritics ASAP 2010 apparatus. The Ni and B contents were determined by inductively coupled plasma-atomic emission spectrometry (ICP-AES, IRIS Intrepid II XSP, Thermo Elemental).

Electrochemical tests

Electrochemical measurements were performed in a three-electrode electrochemical cell on a potentiostat/galvanostat (Reference 600, Gamry Instruments) with a 5 mm diameter glassy carbon (GC) rotating disk electrode (Pine Instruments), a double junction Ag/AgCl (saturated KCl) electrode and a Pt foil as the working, reference and counter electrodes, respectively. All electrode potentials are converted to the reversible hydrogen electrode (RHE) scale according to the Nernst equation: $E_{RHE} = E_{Ag/AgCl} + 0.059pH + 0.197$. The working electrode was prepared as follows. The GC electrode was polished to a mirror finish using aqueous alumina suspensions and cleaned by ultrasonication in deionized water. 5 mg of catalyst (*i.e.*, 3DOM/m Ni, 3DOM Ni, Ni NPs, or commercial Pt/C) was ultrasonically dispersed in 1 mL of 3 : 1 (v/v) water/isopropanol mixed solvent and 40 μL of Nafion solution (5 wt%) for at least 30 minutes to generate a homogeneous ink. A volume of 10 μL of the catalyst ink was then pipetted onto the GC substrate (catalyst loading: ~0.25 mg cm^{-2}) and completely dried.

All electrochemical experiments were conducted in an argon-purged 1.0 M NaOH solution. The linear sweep voltammetry (LSV), beginning at 0.1 V and ending at −0.8 V *vs.* RHE at a scan rate of 2 mV s^{-1}, was conducted with a rotation speed of 2000 rpm after repeating a few times to reach the steady state. Electrochemical impedance spectroscopy (EIS) was performed at an overpotential of 100 mV *vs.* RHE while sweeping the frequency from 5 MHz to 10 mHz at the amplitude of the sinusoidal voltage of 5 mV, and the charge transfer resistances were estimated from the Nyquist plots. The accelerated degradation studies were carried out by cycling the electrode 2000 times and recording the polarization curve after every 200 cyclic voltammetric (CV) sweeps; each cycle started at −0.3 V and ended at +0.2 V *vs.* RHE with a scan rate of 100 mV s^{-1} and a rotational speed of 2000 rpm. The time dependency of catalytic overpotential during electrolysis for the 3DOM/m Ni was tested at a static current density of −10 mA cm^{-2} after equilibrium for 25 hours.

Acknowledgements

The authors gratefully acknowledge financial support from the National Natural Science Foundation of China (51172014 and 20971012), and the National 973 Program of China (2009CB219903).

Notes and references

1 X. B. Chen, C. Li, M. Gratzel, R. Kostecki and S. S. Mao, *Chem. Soc. Rev.*, 2012, **41**, 7909.
2 D. L. Stojic, M. P. Marceta, S. P. Sovilj and S. S. Miljani, *J. Power Sources*, 2003, **118**, 315.
3 M. R. Gao, Y. F. Xu, J. Jiang and S. H. Yu, *Chem. Soc. Rev.*, 2013, **42**, 2986.
4 N. Danilovic, R. Subbaraman, D. Strmcnik, V. R. Stamenkovic and N. M. Markovic, *J. Serb. Chem. Soc.*, 2013, **78**, 2007.
5 F. A. Al-Odail, A. Anastasopoulos and B. E. Hayden, *Phys. Chem. Chem. Phys.*, 2010, **12**, 11398.
6 B. Z. Fang, M. S. Kim, J. H. Kim, M. Y. Song, Y. J. Wang, H. J. Wang, D. P. Wilkinson and J. S. Yu, *J. Mater. Chem.*, 2011, **21**, 8066.
7 N. P. Dasgupta, C. Liu, S. Andrews, F. B. Prinz and P. D. Yang, *J. Am. Chem. Soc.*, 2013, **135**, 12932.
8 J. M. Tang, K. Jensen, M. Waje, W. Z. Li, P. Larsen, K. Pauley, Z. W. Chen, P. Ramesh, M. E. Itkis, Y. S. Yan and R. C. Haddon, *J. Phys. Chem. C*, 2007, **111**, 17901.
9 D. Merki, H. Vrubel, L. Rovelli, S. Fierro and X. L. Hu, *Chem. Sci.*, 2012, **3**, 2515.
10 K. Xiong, L. Li, Z. H. Deng, M. R. Xia, S. G. Chen, S. Y. Tan, X. J. Peng, C. Y. Duan and Z. D. Wei, *RSC Adv.*, 2014, **4**, 20521.
11 A. Lasia, in *Handbook of Fuel Cells – Fundamentals, Technology and Applications*, ed. W. Vielstich, A. Lamm and H. A. Gasteiger, John Wiley & Sons, Ltd., 2003, vol. 2, pp. 416–440.
12 Y. H. Wang, G. X. Zhang, W. W. Xu, P. B. Wan, Z. Y. Lu, Y. P. Li and X. M. Sun, *ChemElectroChem*, 2014, **1**, 1138.
13 K. A. Kuttiyiel, K. Sasaki, W. F. Chen, D. Su and R. R. Adzic, *J. Mater. Chem. A*, 2014, **2**, 591.
14 J. Cai, J. Xu, J. M. Wang, L. Y. Zhang, H. Zhou, Y. Zhong, D. Chen, H. Q. Fan, H. B. Shao, J. Q. Zhang and C. N. Cao, *Int. J. Hydrogen Energy*, 2013, **38**, 934.
15 M. R. Gao, Z. Y. Lin, T. T. Zhuang, J. Jiang, Y. F. Xu, Y. R. Zheng and S. H. Yu, *J. Mater. Chem.*, 2012, **22**, 13662.
16 C. S. Wang, W. Li, X. H. Lu, S. L. Xie, F. M. Xiao, P. Liu and Y. X. Tong, *Int. J. Hydrogen Energy*, 2012, **37**, 18688.

17 J. R. McKone, B. F. Sadtler, C. A. Werlang, N. S. Lewis and H. B. Gray, *ACS Catal.*, 2013, **3**, 166.
18 X. B. Chen, D. Z. Wang, Z. P. Wang, P. Zhou, Z. Z. Wu and F. Jiang, *Chem. Commun.*, 2014, **50**, 11683.
19 A. Walcarius, *Chem. Soc. Rev.*, 2013, **42**, 4098.
20 Y. Yamauchi, A. Tonegawa, M. Komatsu, H. J. Wang, L. Wang, Y. Nemoto, N. Suzuki and K. Kuroda, *J. Am. Chem. Soc.*, 2012, **134**, 5100.
21 Z. X. Wu, Y. Y. Lv, Y. Y. Xia, P. A. Webley and D. Y. Zhao, *J. Am. Chem. Soc.*, 2012, **134**, 2236.
22 Y. Yamauchi, M. Komatsu, M. Fuziwara, Y. Nemoto, K. Sato, T. Yokoshima, H. Sukegawa, K. Inomata and K. Kuroda, *Angew. Chem., Int. Ed.*, 2009, **48**, 7792.
23 L. Ye, Y. Wang, X. Y. Chen, B. Yue, S. C. Tsang and H. Y. He, *Chem. Commun.*, 2011, **47**, 7389.
24 C. H. Wang, C. Yang, Y. Y. Song, W. Gao and X. H. Xia, *Adv. Funct. Mater.*, 2005, **15**, 1267.
25 H. J. Shin, R. Ryoo, Z. Liu and O. Terasaki, *J. Am. Chem. Soc.*, 2001, **123**, 1246.
26 H. J. Wang, H. Y. Jeong, M. Imura, L. Wang, L. Radhakrishnan, N. Fujita, T. Castle, O. Terasaki and Y. Yamauchi, *J. Am. Chem. Soc.*, 2011, **133**, 14526.
27 S. Sattayasamitsathit, Y. E. Gu, K. Kaufmann, S. Minteer, R. Polsky and J. Wang, *Nanoscale*, 2013, **5**, 7849.
28 W. Sugimoto, S. Makino, R. Mukai, Y. Tatsumi, K. Fukuda, Y. Takasu and Y. Yamauchi, *J. Power Sources*, 2012, **204**, 244.
29 Y. Yamauchi, T. Momma, T. Yokoshima, K. Kuroda and T. Osaka, *J. Mater. Chem.*, 2005, **15**, 1987.
30 Y. Yamauchi, S. S. Nair, T. Momma, T. Ohsuna, T. Osaka and K. Kuroda, *J. Mater. Chem.*, 2006, **16**, 2229.
31 G. S. Attard, S. A. A. Leclerc, S. Maniguet, A. E. Russell, I. Nandhakumar and P. N. Bartlett, *Chem. Mater.*, 2001, **13**, 1444.
32 Z. Y. Yuan and B. L. Su, *J. Mater. Chem.*, 2006, **16**, 663.
33 M. Heim, C. Wattanakit, S. Reculusa, C. Warakulwit, J. Limtrakul, S. Ravaine and A. Kuhn, *Electroanalysis*, 2012, **24**, 1.
34 L. H. Nie, A. Y. Meng, J. G. Yu and M. Jaroniec, *Sci. Rep.*, 2013, **3**, 3215.
35 C. M. A. Parlett, K. Wilson and A. F. Lee, *Chem. Soc. Rev.*, 2013, **42**, 3876.
36 J. Jin, L. J. Fu, J. Ouyang and H. M. Yang, *CrystEngComm*, 2013, **15**, 6046.
37 J. Liu, M. Z. Li, J. X. Wang, Y. L. Song, L. Jiang, T. Murakami and A. F. Ujishima, *Environ. Sci. Technol.*, 2009, **43**, 9425.
38 J. Jin, S. Z. Huang, J. Liu, Y. Li, D. S. Chen, H. E. Wang, Y. Yu, L. H. Chen and B. L. Su, *J. Mater. Chem. A*, 2014, **2**, 9699.
39 L. C. Jia, H. Q. Wang, D. Dhawale, C. Anand, M. A. Wahab, Q. M. Ji, K. Ariga and A. Vinu, *Chem. Commun.*, 2014, **50**, 5976.
40 Z. K. Sun, Y. H. Deng, J. Wei, D. Gu, B. Tu and D. Y. Zhao, *Chem. Mater.*, 2011, **23**, 2176.
41 B. L. Su, C. Sanchezl and X. Y. Yang, *Hierarchically Structured Porous Materials*, Wiley-VCH, Weinheim, 2012.
42 N. D. Petkovich and A. Stein, *Chem. Soc. Rev.*, 2013, **42**, 3721.
43 S. C. Warren, L. C. Messina, L. S. Slaughter, M. Kamperman, Q. Zhou, S. M. Gruner, F. J. DiSalvo and U. Wiesner, *Science*, 2008, **320**, 1748.
44 Y. Yamauchi and K. Kuroda, *Electrochem. Commun.*, 2006, **8**, 1677.
45 C. W. Zhang, H. Yang, T. T. Sun, N. N. Shan, J. F. Chen, L. B. Xu and Y. S. Yan, *J. Power Sources*, 2014, **245**, 579.
46 K. S. W. Sing, D. H. Everett, R. A. W. Haul, L. Moscou, R. A. Pierotti, J. Rouquerol and T. Siemieniewska, *Pure Appl. Chem.*, 1985, **57**, 603.
47 T. Saito, E. Sato, M. Matsuoka and C. Iwakura, *J. Appl. Electrochem.*, 1998, **28**, 559.
48 Y. J. Huang, C. H. Lai, P. W. Wu and L. Y. Chen, *J. Electrochem. Soc.*, 2010, **157**, 18.
49 H. Vrubel and X. L. Hu, *Angew. Chem., Int. Ed.*, 2012, **51**, 12703.
50 E. J. Popczun, J. R. McKone, C. G. Read, A. J. Biacchi, A. M. Wiltrout, N. S. Lewis and R. E. Schaak, *J. Am. Chem. Soc.*, 2013, **135**, 9267.
51 P. Xiao, Y. Yan, X. M. Ge, Z. L. Liu, J. Y. Wang and X. Wang, *Appl. Catal., B*, 2014, **154–155**, 232.
52 T. W. Lin, C. J. Liu and C. S. Dai, *Appl. Catal., B*, 2014, **154–155**, 213.
53 S. Baranton and C. Coutanceau, *Appl. Catal., B*, 2013, **136–137**, 1.
54 M. R. Gao, Z. Y. Lin, T. T. Zhuang, J. Jiang, Y. F. Xu, Y. R. Zheng and S. H. Yu, *J. Mater. Chem.*, 2012, **22**, 13662.
55 S. Gu, H. F. Du, A. M. Asiri, X. P. Sun and C. M. Li, *Phys. Chem. Chem. Phys.*, 2014, **16**, 16909.
56 L. Liao, S. N. Wang, J. J. Xiao, X. J. Bian, Y. H. Zhang, M. D. Scanlon, X. L. Hu, Y. Tang, B. H. Liu and H. H. Girault, *Energy Environ. Sci.*, 2014, **7**, 387.
57 L. Liao, J. Zhu, X. J. Bian, L. N. Zhu, M. D. Scanlon, H. H. Girault and B. H. Liu, *Adv. Funct. Mater.*, 2013, **23**, 5326.
58 Z. B. Chen, D. Cummins, B. N. Reinecke, E. Clark, M. K. Sunkara and T. F. Jaramillo, *Nano Lett.*, 2011, **11**, 4168.
59 X. J. Bian, J. Zhu, L. Liao, M. D. Scanlon, P. Y. Ge, C. Ji, H. H. Girault and B. H. Liu, *Electrochem. Commun.*, 2012, **22**, 128.
60 J. Kibsgaard, Z. B. Chen, B. N. Reinecke and T. F. Jaramillo, *Nat. Mater.*, 2012, **11**, 963.
61 B. E. Conway and B. V. Tilak, *Electrochim. Acta*, 2002, **47**, 3571.
62 Y. Choquette, L. Brossard, A. Lasia and H. Menard, *Electrochim. Acta*, 1990, **35**, 1251.
63 N. Krstajic, M. Popovic, B. Grgur, M. Vojnovic and D. Sepa, *Electroanal. Chem.*, 2001, **512**, 16.
64 W. C. Sheng, H. A. Gasteiger and Y. Shao-Horn, *J. Electrochem. Soc.*, 2010, **157**, 1529.
65 D. H. Youn, S. Han, J. Y. Kim, J. Y. Kim, H. Park, S. H. Choi and J. S. Lee, *ACS Nano*, 2014, **8**, 5164.
66 O. H. Kim, Y. H. Cho, S. H. Kang, H. Y. Park, M. Kim, J. W. Lim, D. Y. Chung, M. J. Lee, H. Choe and Y. E. Sung, *Nat. Commun.*, 2013, **4**, 2473.

67 R. Y. Zhang, D. K. Shen, M. Xu, D. Feng, W. Li, G. F. Zheng, R. C. Che, A. A. Elzatahry and D. Y. Zhao, *Adv. Energy Mater.*, 2014, **4**, 1301725.
68 T. Y. Ma, S. Dai, M. Jaroniec and S. Z. Qiao, *J. Am. Chem. Soc.*, 2014, **136**, 13925.
69 Z. C. Xing, Q. Liu, A. M. Asiri and X. P. Sun, *Adv. Mater.*, 2014, **26**, 5702.
70 C. Z. Yuan, J. Y. Li, L. R. Hou, J. D. Lin, X. G. Zhang and S. L. Xiong, *J. Mater. Chem. A*, 2013, **1**, 11145.
71 M. Gong, W. Zhou, M. C. Tsai, J. G. Zhou, M. Y. Guan, M. C. Lin, B. Zhang, Y. F. Hu, D. Y. Wang, J. Yang, S. J. Pennycook, B. J. Hwang and H. J. Dai, *Nat. Commun.*, 2014, **5**, 4695.
72 E. J. Popczun, C. G. Read, C. W. Roske, N. S. Lewis and R. E. Schaak, *Angew. Chem., Int. Ed.*, 2014, **53**, 5427.
73 R. W. Liu, S. Gu, H. F. Du and C. M. Li, *J. Mater. Chem. A*, 2014, **2**, 17263.
74 H. W. Shim, A. H. Lim, J. C. Kim, E. Jang, S. D. Seo, G. H. Lee, T. D. Kim and D. W. Kim, *Sci. Rep.*, 2013, **3**, 2325.
75 S. H. Sun, G. X. Zhang, D. S. Geng, Y. G. Chen, R. Y. Li, M. Cai and X. L. Sun, *Angew. Chem., Int. Ed.*, 2011, **50**, 422.
76 S. X. Cai, D. S. Zhang, L. Y. Shi, J. Xu, L. Zhang, L. Huang, H. R. Li and J. P. Zhang, *Nanoscale*, 2014, **6**, 7346.
77 Y. W. Tan, P. Liu, L. Y. Chen, W. T. Cong, Y. Ito, J. H. Han, X. W. Guo, Z. Tang, T. Fujita, A. Hirata and M. W. Chen, *Adv. Mater.*, 2014, **26**, 8023.
78 R. C. Schroden, M. Al-Daous, C. F. Blanford and A. Stein, *Chem. Mater.*, 2002, **14**, 3305.